FLOW ANALYSIS AND DRAG PREDICTION FOR TRANSONIC TRANSPORT WING/BODY CONFIGURATIONS USING A VISCOUS-INVISCID INTERACTION TYPE METHOD*

J. van Muijden**, A.J. Broekhuizen***,
A.J. van der Wees†, J. van der Vooren‡

National Aerospace Laboratory NLR
P.O.BOX 90502
1006 BM Amsterdam
The Netherlands
Tel: (020)5113113; Fax:(020)5113210

ICAS-94-2.6.5

Abstract

A CFD method is described for transonic drag prediction of wing/body configurations that are representative for new commercial transport aircraft. The objective is to demonstrate that this CFD method satisfies two essential requirements:
(i) CFD-problem-turnaround-time (including grid generation) of the order of a day to a week, or less, and
(ii) high accuracy of aerodynamic forces, such as transonic drag-creep.
Accuracy requirements currently used are those that have been formulated for wind tunnel experiments. The demonstration that realistic accuracy requirements are met is based on a comparison between computed results and experimental data for
(i) surface pressure distributions on wing sections,
(ii) transonic drag-creep curves (drag coefficient versus Mach number at fixed lift coefficient and Reynolds number), and
(iii) transonic drag rise Mach numbers,
for a series of geometrically and aerodynamically different wing/body configurations. It is shown that the CFD results are accurate in terms of drag rise Mach number, while drag-creep data increments predicted for different wing/body configurations are consistent with the experimental drag-creep data increments.

1 Introduction

1.1 Background

The needs of aerospace industry in CFD technology, as derived from aerodynamic design objectives for new commercial transport aircraft, can be formulated in terms of requirements to be satisfied by CFD methods and supercomputers. For CFD technology to have an impact on the aerodynamic design of airplanes,

CFD-problem-turnaround-time (incl. grid generation) must be of the order of a day to a week, or less. Aerodynamic analysis is a process of looking at a significant number of flow conditions (lift coefficients, Mach numbers, Reynolds numbers) for more than one geometric variant, such that a large number of runs has to be made. If CFD methods do not yield results at this industrial time scale the impact on the aerodynamic design will be reduced.

A second requirement which needs to be met by CFD tools for the development of commercial transport aircraft is high accuracy of aerodynamic forces, such that the computed drag, pitching moment and lift can be relied upon to reduce the risks involved in airplane design. This second requirement translates for example into better turbulence models and extreme grid resolution, such that grid convergence is obtained. Current accuracy requirements are derived from those formulated for wind tunnel experiments by Steinle and Stanewsky[1]. The most stringent requirement is that drag increments due to minor changes in configurations should be accurate up to 0.0001 in the drag coefficient (one count). If the drag rise Mach number is defined as the Mach number at which the drag rises at a rate of 0.05 ($dC_D/dM = 0.05$ at fixed lift coefficient and Reynolds number), it is found that the drag rise Mach number increment due to minor changes in configurations should be accurate up to 0.002.

It is clear, however, that the above requirements for aerodynamic data accuracy as set forth in AGARD Advisory Report 184[1] are seldom met in experimental investigations, as concluded by McCroskey[2] for NACA 0012 airfoil data and as demonstrated by Boersen and Elsenaar[3] for testing with half-span models. For transonic drag assessment more realistic data accuracy requirements are plus or minus 3 counts for drag increments, and therefore plus or minus 0.006 in drag rise Mach number increments.

The problem-turnaround-time requirement for analysis of three-dimensional configurations covering the complete lift, Mach and Reynolds number range cannot be met by Reynolds- averaged Navier-Stokes methods at present. The use of less sophisticated flow models during the design phase is therefore widely accepted in order to satisfy the problem-turnaround-time requirement, although the accuracy of the results still has to satisfy the second requirement. An example of the application of comparatively simple flow models to airfoil and wing design can be found in the work of Henne and Gregg [4]. They managed to predict the effects of an unconventionally shaped trailing edge on the transonic drag-creep behaviour, using an inviscid full-potential method in three dimensions, and a coupled viscous-inviscid method for two-dimensional airfoil analysis, leading to an improved wing concept. The computationally found improvement in the transonic drag-creep was later confirmed by wind tunnel experiments. Thus, this reference shows the effectiveness of applying comparatively simple flow models to a wide variety of configurations during design studies. The present viscous-inviscid flow solver, to be described in the next sections, is similarly intended to be used as an analysis tool during the design phase for transonic wing/body configurations, with particular emphasis on drag prediction.

1.2 Inviscid flow drag

Van der Vooren et al. [5][6] have used an inviscid full-potential method to compute both near-field and far-field drag. Near-field drag is obtained from the integration of surface pressures. Far-field drag consists of induced drag and wave drag. Induced drag is easily calculated from classical Trefftz-plane analysis. Wave drag is determined by integration of artificial viscosity in supersonic flow regions (an approach originated earlier by Garabedian [7]), supplemented by a momentum deficit insofar as captured shock waves extend into subsonic flow regions downstream.
Destarac [8] has also used an inviscid full-potential method. For the determination of wave drag a computation of the momentum deficit in supersonic and subsonic flow regions is used, applied at suitably chosen grid planes surrounding the shock waves. Applying the method to a wing with elliptic loading, it is shown that the far-field approach is more accurate than the near-field integration of surface pressures. This finding is also reported by Van der Vooren and Van der Wees [6].
A similar effort to compute inviscid drag by evaluating induced drag and wave drag, this time using Euler methods, has been undertaken by Nikfetrat et al. [9]. The components are obtained by integrating the trailing edge vorticity (induced drag) and the entropy rise across the shocks (wave drag) at suitably chosen planes. Again, these values are compared to the values obtained from surface pressure integration. It is shown that the integration of trailing vorticity leads to more accurate

drag values for subsonic flow conditions than the surface pressure integration.

1.3 Viscous flow drag

For realistic drag predictions, however, the viscous contribution to the total drag value needs to be taken into account. For a complete understanding of the origin of drag, all major physical components (i.e. wave, induced and viscous drag) have to be made available, assuming that the interaction between these components is negligibly small.
In the present viscous-inviscid flow solver, both near- and far-field drag is calculated. Near-field drag comprises both pressure drag and friction drag as obtained from surface integration. However, pressure drag suffers from numerical inaccuracies in a similar manner as experienced for inviscid flow methods. Far field drag comprises induced drag, wave drag and viscous drag. Induced drag is calculated from classical Trefftz-plane analysis. Wave drag is calculated following Van der Vooren and Van der Wees [6]. Viscous drag is calculated from the boundary layer momentum thickness of the wake behind the wing.
A great advantage of using a viscous-inviscid interaction method for drag-prediction purposes is the natural subdivision of the far- field drag into its relevant physical drag components. So far, Reynolds-averaged Navier-Stokes methods have only been capable of producing integrated pressure and friction drag values, where the former is subject to the errors involved in near-field drag evaluation. The inherent interaction of boundary layers with shock waves and with trailing vorticity makes it more difficult to differentiate between induced, wave and viscous drag values in Navier-Stokes methods.

2 Description of methodology

2.1 Scope

The present flow solver is a viscous-inviscid interaction type method developed at NLR, consisting of a full-potential solver, a boundary layer solver and a viscous-inviscid strong interaction algorithm [10]. The method is in use for the calculation of the influence of wing boundary layer and wake on the inviscid flow about a given wing/body configuration at subsonic and transonic speeds. Apart from the calculation of pressure distributions for viscous wing flow, the method is intended to provide lift and drag data for complete wing/body configurations.
The method is capable to do computations for prescribed angle of attack, but also for prescribed total lift coefficient. The method is also suitable for off-design studies. Since the viscous and inviscid methods are strongly coupled, at least moderate boundary layer separation can be handled, thus yielding opportunities for buffet-onset prediction, shock wave/boundary layer interaction studies or, in the lower Mach number

regime, indication of the onset of boundary layer separation at the trailing edge at high angles of attack.

The method provides useful information when analyzing wind tunnel and/or flight test data. In this respect, the prediction of Reynolds number effects is important for new aircraft designs. When only wind tunnel data are available, the method can be used to obtain an extrapolation towards full scale Reynolds numbers.

For quick interpretation of results, the method has been supplemented with powerful automated postprocessing facilities, capable of providing a set of data sheets and user-defined figures of relevant flow quantities at prescribed wing stations.

2.2 Grid generation

The present flow solver makes use of grids, generated by an algebraic grid generator[11]. The grids are boundary-conforming, using a C-O topology; a complete wing/body configuration is captured in one single block. The position of the wake cut behind the wing is fixed. A typical example grid is shown in figure 1. This grid is not keelline-conforming, where the keelline is the intersection of the body and the symmetry plane.

A fixed setting of input parameters is used in order to obtain grids of sufficient quality for most geometries. Grid generation and inspection requires about an hour of man-power, and has become a routine matter.
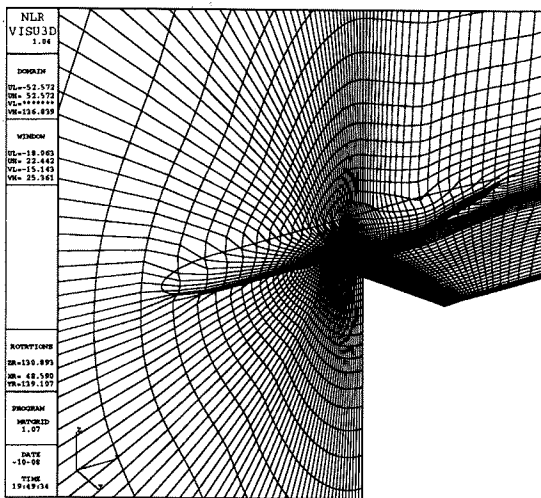
Fig. 1a   Computational grid on the wing, its wake, the body and the symmetry plane

2.3 Full-potential solver

The full-potential solver employs a fully-conservative finite-volume scheme in a curvilinear coordinate system. The scheme is second-order accurate, except near shocks, where the accuracy reduces to first order. At supersonic-subsonic shock waves, the solver offers an option to choose between a fully-conservative and a non-conservative shock representaion. This switch influences the strength of the computed shock wave, yielding mass-conservation in case of the fully-conservative option and artificial mass-production in case of the non-conservative option. The non-conservative option
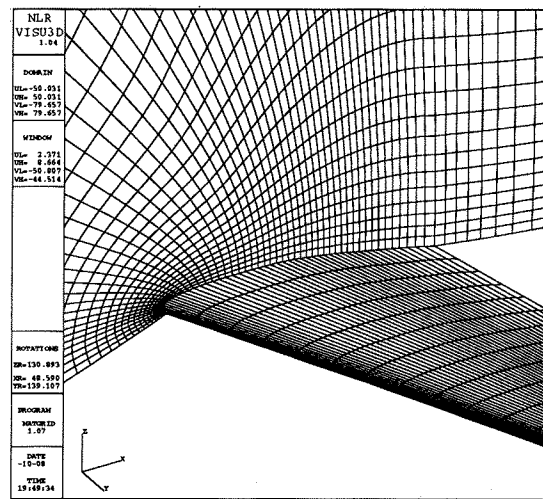
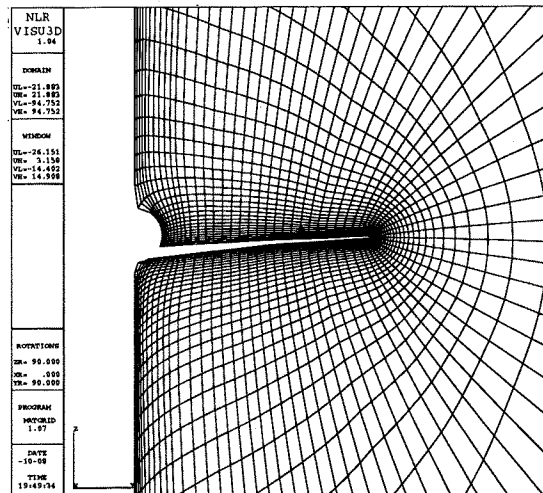**Fig. 1b   Side view of wing-normal grid plane**

Fig. 1c   Detailed view of the wing grid and a stream-normal grid plane

does not influence the mass-conservation in the flow field away from shock waves. The set of discretized equations is solved using a multigrid method and an ILU/SIP smoothing algorithm[12].

2.4 Viscous solver

The basis for the viscous solver is formed by the unsteady first-order boundary layer equations in integral form. These equations, reflecting conservation of mass and momentum, have to be supplemented with an algebraic velocity-density relation as a suitable approximation to the solution of the energy equation along a surface normal, and with closure relations, derived from a family of theoretical velocity profiles and empirical turbulent boundary layer data correlations, in order to reduce the number of unknowns to four. Both laminar and turbulent closure relations are prescribed, also using an extended Granville transition criterion[13] to determine free-transition. Fixed transition is possible by prescribing a local Reynolds number based on momentum thickness at a prescribed transition line. In the present

results, a value of 320 has been taken. At present, turbulent closure relations are not obtained from velocity profiles, but adapted closure relations taken from two-dimensional methods[14][15] have been used instead. Laminar closure relations, derived from the self-similar Falkner-Skan velocity profiles, have been given by Cousteix[13]. The viscous flow is solved on the wing and its wake only; the boundary layer on the fuselage is not computed.

The boundary layer solver uses a prescribed velocity distribution obtained from the inviscid solver, and is as such a direct solution method. In order to avoid break-down of the boundary layer equations at flow separation, induced by unrealistic velocity gradients, an extra equation is needed to adapt the velocity distribution during the iteration process. This so-called interaction law is a rough approximation to the inviscid flow equation, which is reshaped to fit into the set of boundary layer equations. By implementing the interaction law as a correction equation, no influence is exerted on the final converged viscous-inviscid solution. First-order accurate discretization in space of the boundary layer equations is done with respect to the direction of the characteristics using a matrix-split procedure[16]. An implicit backward-Euler time-integration scheme is used to obtain a steady-state solution of the discretized equations.

The surface grid of the full-potential solver is used in the boundary layer computation.

For a detailed description of the boundary layer solver, see Van der Wees and Van Muijden[10].

2.5 Viscous-inviscid interaction algorithm

The above described inviscid full-potential solver and viscous boundary layer solver are strongly coupled using a quasi-simultaneous interaction algorithm[17]. The organisation of the coupling is shown in figure 2. Regarding a fully simultaneous coupling method as the most natural option available, the quasi-simultaneous coupling method is judged to be second-best based on the ability to compute converged solutions with modest effort. The quasi-simultaneous method is reasonably easy to implement since it does not affect the individual solution methods of the inviscid and viscous solvers. The quasi-simultaneous coupling method results in a convergence speed penalty for difficult flow conditions with extensive boundary layer separation, as has been shown earlier[12].

2.6 Drag prediction

Drag is predicted by calculating on a sequence of three nested grids, with (nominal) mesh sizes in the ratios 1, 2/3 and 1/2, where the ratios are defined with respect to the coarse grid. Here the coarse grid (mesh size ratio 1) has about 200,000 grid points, and produces representative pressure distributions. Consequently, the medium grid (mesh size ratio 2/3) has about 675,000 grid points, and the finest grid (mesh size ratio 1/2) about 1,600,000

grid points. Experience has shown that numerically accurate values for the drag, either at fixed incidence or at fixed lift, are obtained in the limit of zero mesh size, i.e. for zero discretization error. With the present method this grid convergence is achieved by a linear extrapolation procedure. However, drag values on each grid are subject to scatter caused by grid properties, implementation details and non-perfect convergence. This introduces scatter in the extrapolated values. See figure 3a.
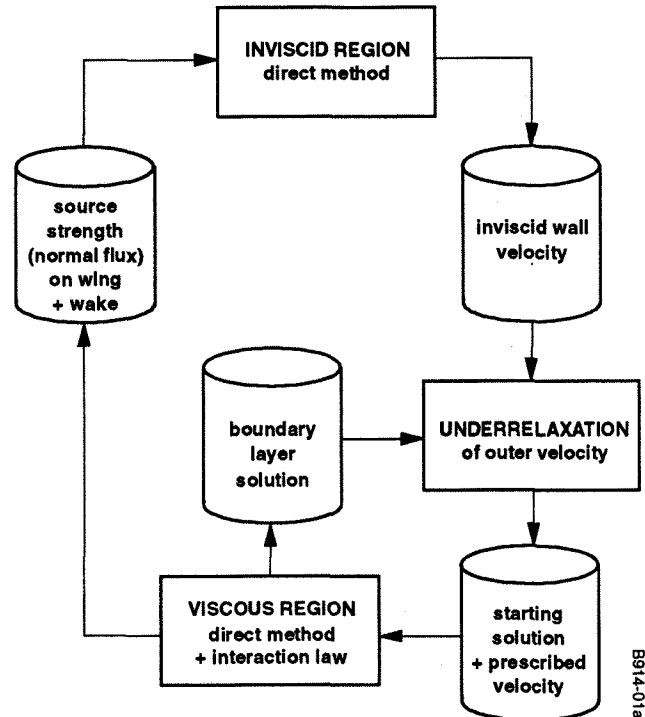

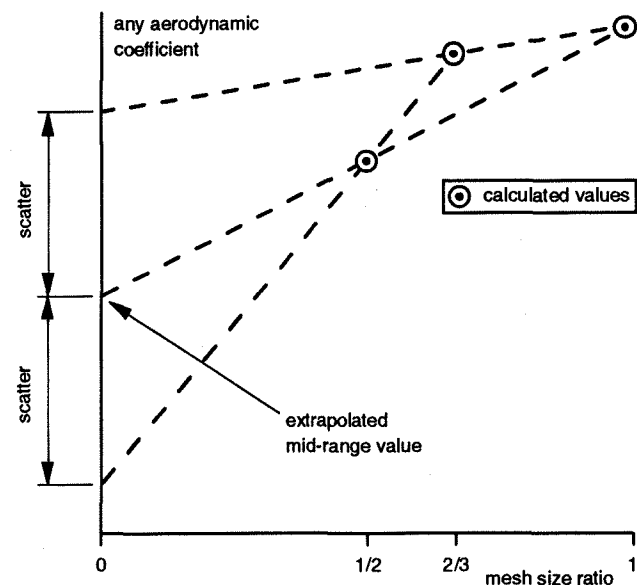Fig. 2   Description of quasi-simultaneous interaction algoritm

Fig. 3a   Origin of scatter in extrapolated value for linear grid dependency

1931

As observed from computations for various research wing/body configurations, the average scatter up to the drag-divergence Mach number does not exceed about plus or minus 3 counts for extrapolated total drag and total drag-creep, while incidental peak values do not exceed 5 counts. See figures 3b,c.
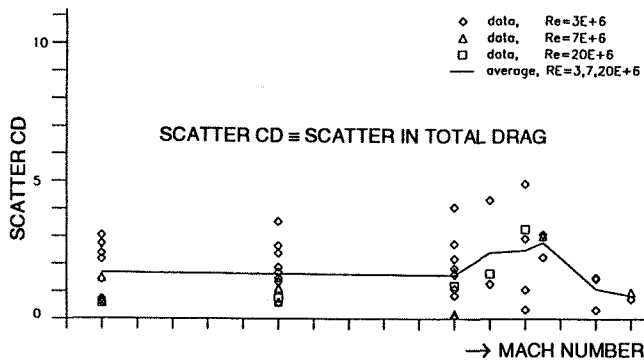

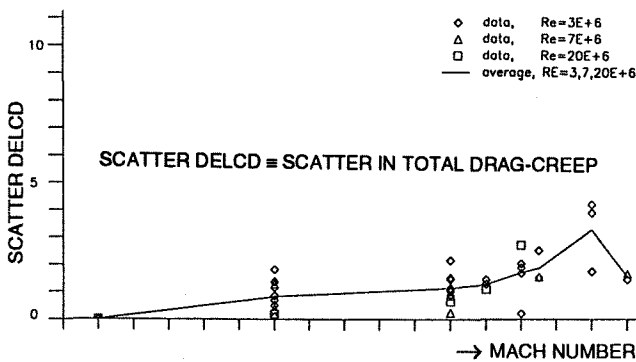Fig. 3b   Scatter in extrapolated drag data

Fig. 3c   Scatter in extrapolated drag data

On the finest grid, the scatter is lowest and is in fact four times lower than for the extrapolated values, under the assumption that the scatter on a particular grid is of the order of the mesh size. The grid extrapolation procedure is applied to each far-field component, induced drag, viscous drag and wave drag, and also to the total drag as the sum of these components.

A point of attention, apart from the numerical accuracy of the computed drag data, is the dependency of computational drag on the turbulence modelling. In figure 4, computational drag results are shown for the CAST-7 airfoil[18], using the ISES flow solver[19]. Several drag curves are obtained for the same configuration at the same flow conditions, using modified relations in the turbulent viscous model. The computed drag values differ up to 10 counts at transonic flow conditions. This example gives an idea about the range of answers that can be produced within the uncertainty of turbulence modelling. The present method, employing an integral boundary layer description which is similar to ISES, is therefore likely to yield drag predictions sensitive to changes in the turbulent viscous model. Thus, differences between measured and computed drag data are, at least partly, due to uncertainties in turbulence modelling.
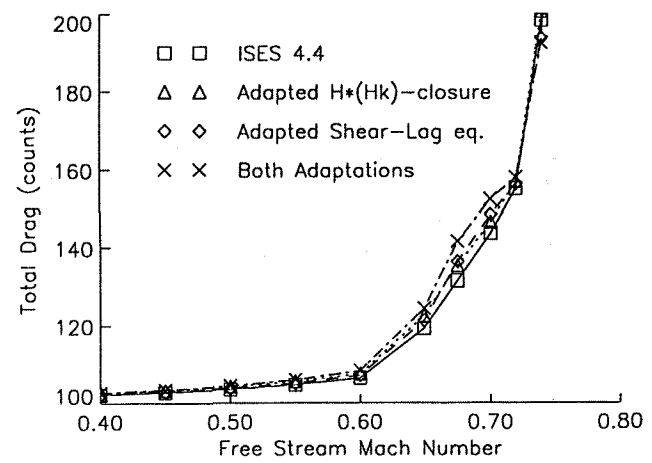

Fig. 4   Drag computations for the CAST - 7 airfoil at $C_L = 0.8$, $Re = 3.2*10^6$, transition at 5% chord, using different viscous models in ISES

2.7 Computational performance

The method has been tested extensively for many configurations and many flow conditions. Experience has shown that the robustness of the quasi-simultaneous viscous-inviscid strong interaction method is favourable. Using, in each viscous-inviscid iteration step, one multigrid cycle in the inviscid solver and five time steps in the viscous solver, the final converged solution is obtained in 30 viscous-inviscid iteration steps for attached boundary layer flow. For separated flow conditions, the effort needed to obtain convergence can amount to 2-3 times as many viscous-inviscid iteration steps, depending on the extent of separated flow.

On a grid with 200,000 grid points the computation time is 5 minutes on a single processor of the NLR NEC-SX3/22 super-computer, at an equivalent computational speed of 200 MFLOPS. Compared to Reynolds-averaged Navier- Stokes methods, the turnaround-time of the present method is at least one order smaller. Regarding the grid generation process, the turnaround-time for the generation of a full-potential grid is also at least one order smaller than for the generation of a Navier-Stokes grid. Thus, the required problem-turnaround-time for analysis of three-dimensional configurations covering the complete lift, Mach and Reynolds number range (requiring of the order of 60 to 90 flow conditions) cannot at present be met by Euler/Navier-Stokes technology. As a result, methods based on full-potential and boundary layer technology continue to be of importance, in particular if they combine short turnaround-times with reliable drag prediction capabilities.

The CFD-problem-turnaround-time for viscous drag prediction with the present method is currently in the order of less than a week

3 Applications

3.1 Pressure distributions

The results shown here are obtained on the coarse grid (mesh size ratio 1) of 160 by 40 by 32 grid points in streamwise, spanwise and wing-normal direction respectively. The coarse grid was chosen to demonstrate that representative pressure distributions do not require such high-resolution as does drag prediction (compare section 2.6). The conservative shock operator is used.

DLR-F4 wing/body

The DLR-F4 wing/body configuration has been designed as a simple but realistic transport aircraft type configuration with a high aspect-ratio transonic wing. A wind tunnel model of the DLR-F4 wing/body has been tested in three European wind tunnels, yielding pressure distributions and force measurements[20]. The DLR-F4 wing/body appears to be a difficult test case for CFD methods due to the severe rear-loading and the finite trailing edge thickness. In the present method, a finite trailing edge thickness is extended into a finite wake cut gap in the grid, extending from the trailing edge to the downstream boundary. In figure 5 computed pressure distributions are compared with experimental data at selected spanwise stations. The flow condition for this case is a lift coefficient of 0.6, a Mach number of 0.75 and a Reynolds number of 3 million. Transition was fixed at positions varying between 5 and 25 percent chord. On the inboard part of the wing, a double shock is present in the experimental data. This double shock is difficult to capture computationally due to its orientation, which does not coincide with the grid lines. The occurrence and strength of the forward shock in the experiments seem to be influenced by the forced transition closely ahead of the forward shock.
On the outer part of the wing, a single shock occurs. The computed position is quite accurate, except at the most outboard section. An explanation of this difference can possibly be found in the lack of three-dimensional viscous modelling. A good approximation of the converging cross flow in the boundary layer behind the shock on the outboard wing will move the shock at the wing tip to a position which is in better agreement with the experiment. However, considering the comparatively simple turbulence modelling, the overall agreement is acceptable for this severe test case.

Fokker 100 wing/body

The flow about the Fokker 100 wing/body configuration has been computed at transonic free stream conditions, serving as a real industrial test case. Two different Reynolds numbers have been taken, one for wind tunnel conditions, the other for flight test conditions. The geometry, defined for the wind tunnel model, has been taken unchanged as input for the grid generator. For the flight test computation, the wind tunnel geometry has been taken as the basic geometry, but the wing deformation in flight has been estimated and accounted for by adding an extra wing twist distribution along the span. Thus, a second grid, different from the first, was generated in order to avoid possible discrepancies in the comparisons of pressure distributions with experimental data due to geometrical differences.
For the wind tunnel test, the free stream Mach number is 0.779, the angle of attack is 1.03 degrees and the Reynolds number is 2.9 million. Transition was fixed at 5 to 7 percent chord. For the flight test, the free stream Mach number equals 0.775, at an angle of attack of 1.0 degrees and a Reynolds number of 35 million. Transition is assumed to occur at approximately 5 percent chord. Both flow cases are beyond the design cruise condition resulting in strong shock wave/boundary layer interaction. In figure 6 two pressure distributions at selected spanwise stations are compared with experimental data for both test cases. Looking at the free flight test case, the comparison with experimentally obtained data is quite good. The position of the shock wave is acceptably predicted, while also the general shape of the pressure distributions is accurately captured. On the upper side of the wing, the level of the pressure coefficient upstream of the shock is slightly mispredicted. Note that the experimental pressure distributions are less smooth than those from the wind tunnel experiment. This may be a result of the disturbance of the flow due to the pressure belts wrapped around the wing.
The wind tunnel test case has been computed using the Mach number and the angle of attack of the experiment without any corrections. The comparison of pressure distributions with experimental data is quite acceptable, giving a good pressure level at the upper side of the wing, although now the position of the shock wave is not predicted as accurately.

3.2 Drag-creep consistency

The drag-creep at a given Mach number is defined by the increase in total drag coefficient relative to the total drag value at a reference Mach number, at fixed lift coefficient and Reynolds number. Drag-creep consistency is investigated on the fine grid (mesh size ratio 1/2) of 320 by 80 by 64 grid points in streamwise, spanwise and wing-normal direction respectively. The fine grid was chosen because then the scatter is lowest, while the results are also closest to the extrapolated results. The conservative option was once more chosen in order to avoid numerical uncertainties in wave drag due to artificial mass-production that might reduce the consistency of the results.

DLR-F4 wing/body

An example of computed drag-creep is shown in figure 7 for the DLR-F4 wing/body. Here, computed drag-creep results are compared with experimental data from three wind tunnels, at a lift coefficient of 0.5 and a
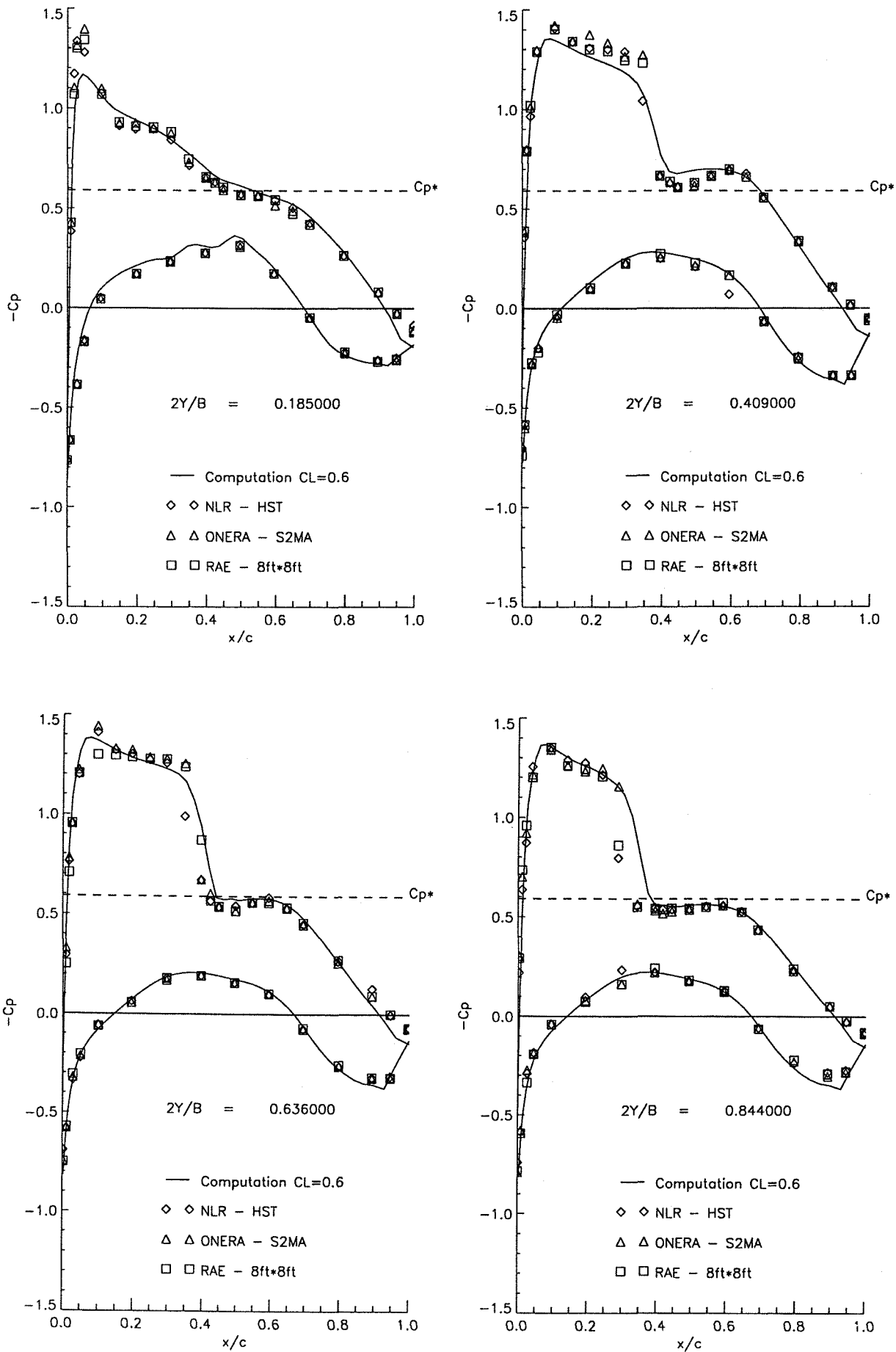
Fig. 5 Comparison of computed and measured chordwise pressure distributions on four wing sections of the DLR - F4 wing/body at $M_\infty = 0.75$, $C_L = 0.6$, $Re = 3*10^6$
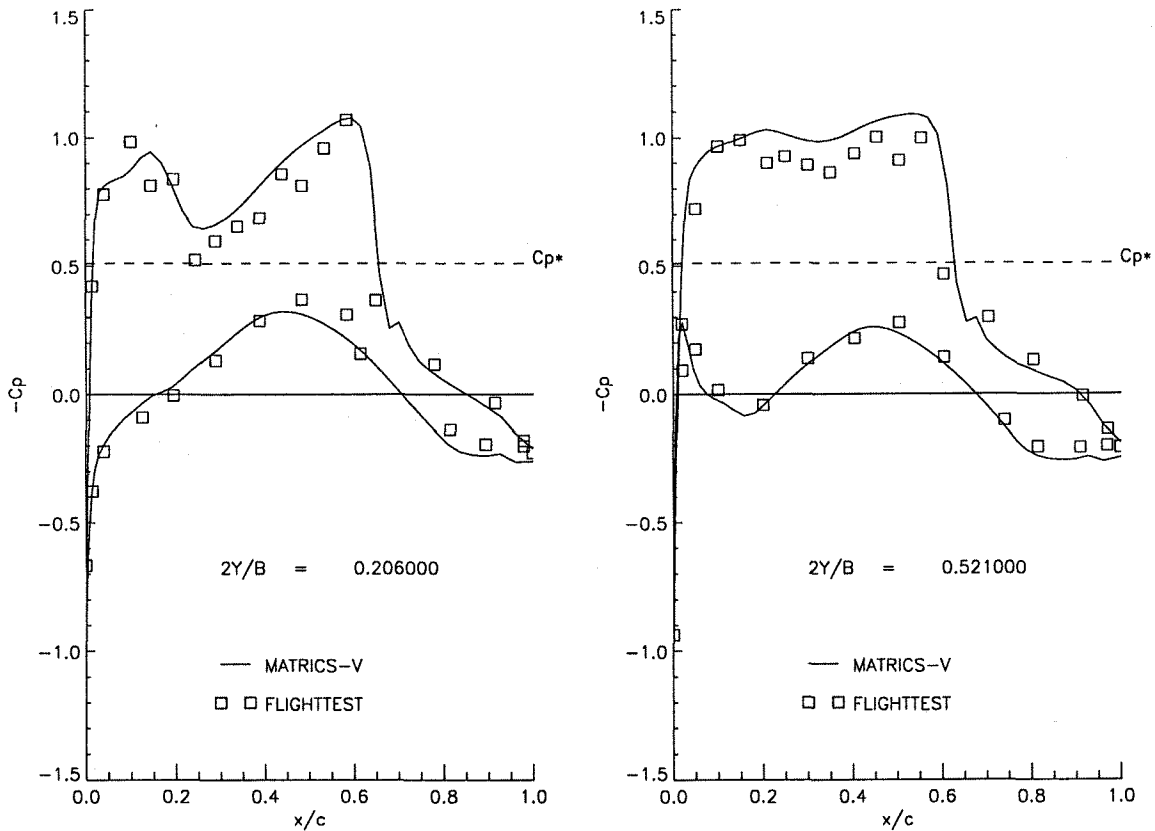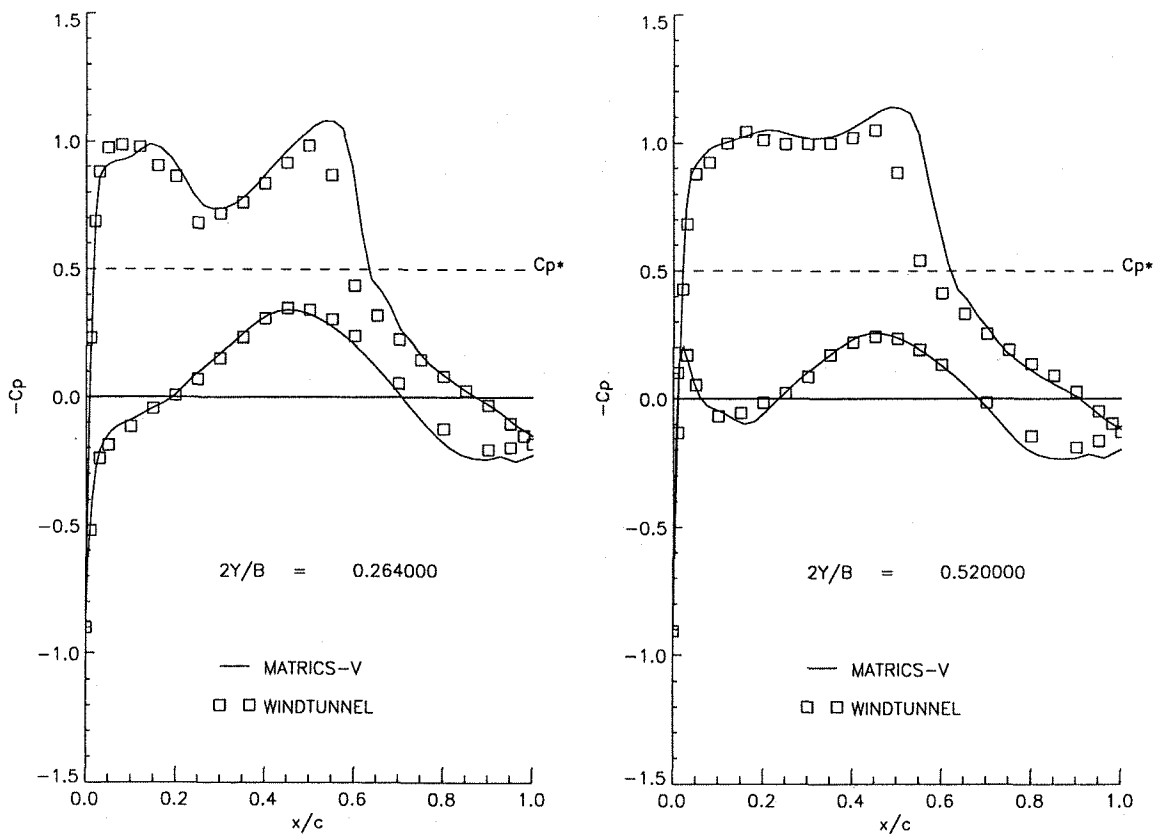
Fig. 6a   Comparison of computed and measured chordwise pressure distributions on two wing sections of the Fokker 100 wing/body at $M_\infty = 0.775$, $\alpha = 1°$, $Re = 35*10^6$

Fig. 6b   Comparison of computed and measured chordwise pressure distributions on two wing sections of the Fokker 100 wing/body at $M_\infty = 0.779$, $\alpha = 1.03°$, $Re = 2.9*10^6$

Reynolds number of 3 million. The computed data appear to be consistently lower than the experimental data.

Understanding of the various sources of drag is obtained by analyzing the spanwise distributions of wave drag and viscous drag, and the chordwise spatial distributions of wave drag. An example is given in figures 8a, 8b for the present DLR-F4 wing/body computations at a freestream Mach number of 0.75. For this case, a correlation is evident between the local strength of the shock wave and the local thickening of the boundary layer (figs. 8a,b). In figure 8c, the spatial distribution of wave drag is plotted at a chordwise section on the outer part of the wing, showing the height of the local shock. Such diagnostic plots are helpful to understand drag differences between configurations.

Fokker 100 wing/body

For transonic drag-creep, qualitatively consistent behaviour is found with variation of Reynolds number and Mach number for the Fokker 100 wing/body as shown in figure 9. In figure 9a, the computed drag-creep is plotted. As expected, the drag-creep is lowest for the higher Reynolds number. Also shown, in figure 9b, are the experimentally obtained drag-creep data, derived from wind tunnel tests and flight experiments. Qualitatively, the computed Reynolds and Mach number influence is consistent with experiments.

Statistical correlation

Recently, computations have been performed with the present method for a number of geometrically and aerodynamically different research wing/body configurations, including the DLR-F4 wing/body. Drag-divergence Mach numbers, obtained from experiments, have been compared with the drag-divergence Mach numbers extracted from the computed drag-creep curves. The drag-divergence Mach number is defined as the Mach number where the drag coefficient rises at a rate of 0.05. Usually, a somewhat higher value for the rate is taken, rendering the present estimate of the drag-divergence Mach number conservative. In figure 10a the computed and experimental drag-divergence Mach numbers are plotted showing fair statistical correlation between experiment and computation. The computed drag-creep values at the drag-divergence Mach number have been correlated with their experimental counterparts for full-span wind tunnel models in figure 10b and for half-span wind tunnel models in figure 10c. Here, the correlation is again fair, but it is found that the computed drag-creep is systematically lower than the experimental values. The above correlations lead to the conclusion that different wing designs can be compared, using the present method, by doing computations on the fine 320 by 80 by 64 grid (mesh size ratio 1/2). Once a design is selected, the grid extrapolation procedure must be applied to calculate accurate final drag values (compare section 2.6).

4 Concluding remarks

A CFD method has been described for transonic drag prediction of wing/body configurations that are representative for new commercial transport aircraft. The method is based on an algebraic grid generator, an inviscid flow solver for the full-potential equation, a viscous flow solver for the boundary layer equations, and a viscous-inviscid interaction algorithm.

The method has been tested extensively for a significant number of geometrically and aerodynamically different wing/body configurations. It is found that the method satisfies two essential requirements:

(i) CFD-problem-turnaround-time of the order of a day to a week for a significant number of flow solutions; the grid generation process is standardized and automated to a large extent, while the NLR NEC-SX3/22 supercomputer is exploited to obtain high computational speed.

(ii) realistic accuracy of aerodynamic forces, such as transonic drag creep.

The demonstration that realistic accuracy requirements are met is based on a comparison between experimental data and computed results for pressure distributions on wing sections, transonic drag-creep curves at fixed lift coefficient and fixed Reynolds number, and transonic drag-rise Mach numbers. The computational results indicate that representative pressure distributions on wing sections can be obtained on grids with 200,000 grid points. Transonic drag computation is, however, an exacting task due to the sensitivity of drag values to numerical approximations, convergence levels and turbulence modelling (including transition strip modelling). Computational experiments on grid sequences have lead to the observation that up to approximately 1,600,000 grid points are required to predict transonic drag-creep increments (between geometrically different wing/body configurations) with an accuracy of plus or minus 3 counts of the extrapolated total drag-creep value at the drag-divergence Mach number.

The development of this transonic drag prediction capability is claimed to be a significant step forward. The ability of the present method to distinguish between the three basic drag components (viscous, induced and wave drag) and to determine their spanwise distributions allows the aerodynamic designer to make minor modifications to improve the overall three-dimensional design.

Future improvements to the method, with the objective of meeting further industrial requirements, are foreseen in the viscous modelling, but also in the attainable convergence level. This will improve the accuracy of drag data without increasing the computational effort. Improved convergence levels for a given number of interaction steps are in fact mandatory for off-design studies at flow conditions including boundary layer separation (buffet-onset). The resolution of the boundary layer on the body will not be incorporated in the present method. For this purpose, Navier-Stokes methods are available. In the future, a far-field drag decomposition methodology will also be defined for Navier-Stokes

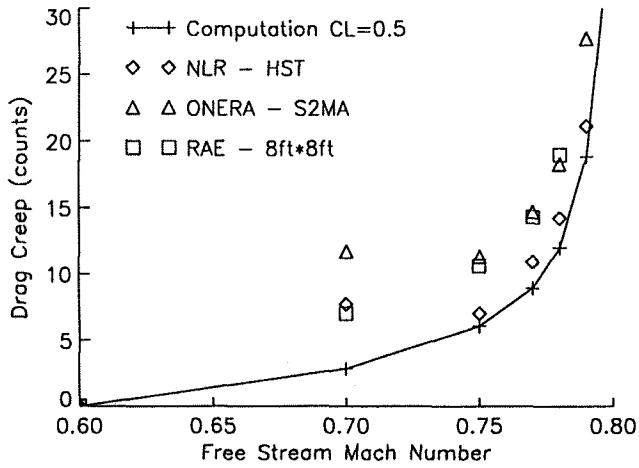methods, using the experience obtained with the present interaction type method.

Fig. 7   Comparison of computed and measured drag-creep for the DLR - F4 wing/body at $C_L = 0.5$, $Re = 3*10^6$; transition fixed at 5 - 25% chord
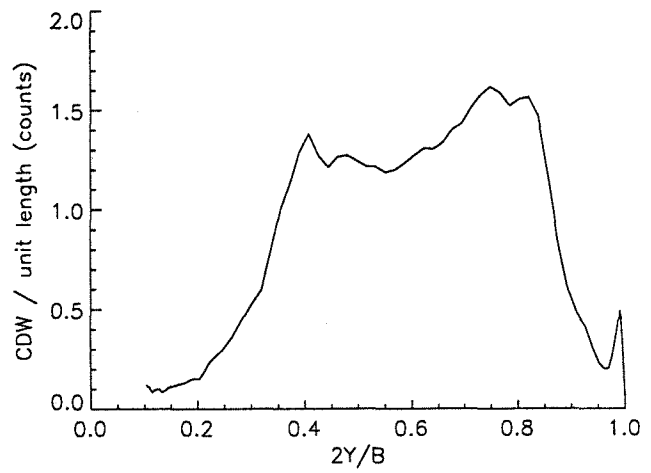

Fig. 8a   Spanwise distribution of wave drag for the DLR - F4 wing/body at $M_\infty = 0.75$, $C_L = 0.5$, $Re = 3*10^6$
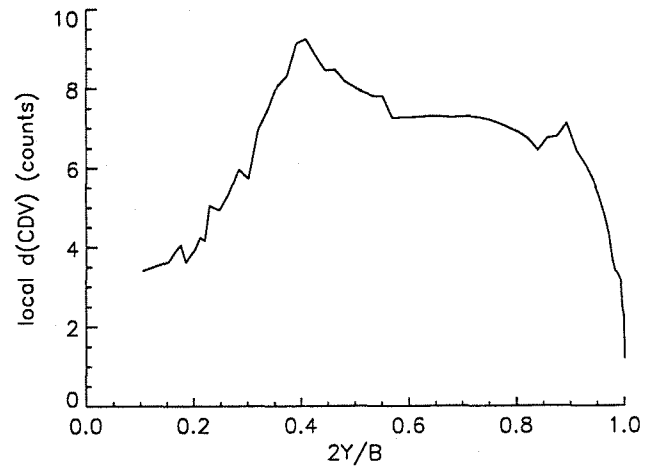

Fig. 8b   Spanwise distribution of viscous drag-creep between $M_\infty = 0.60$ and $M_\infty = 0.75$ for the DLR - F4 wing/body at $C_L = 0.5$, $Re = 3*10^6$
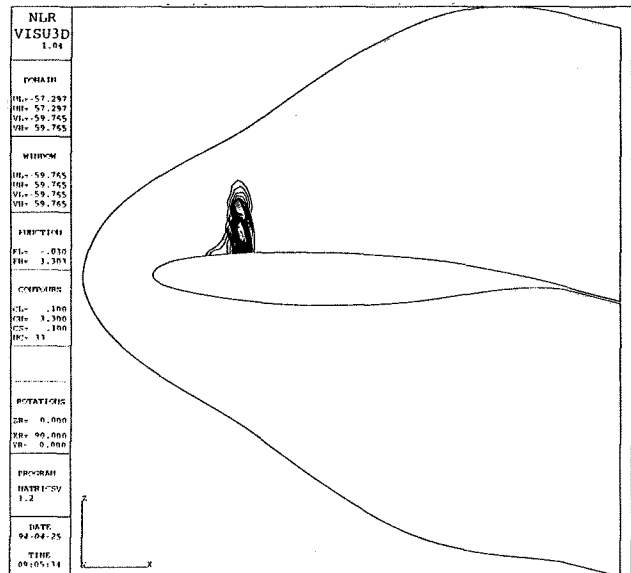
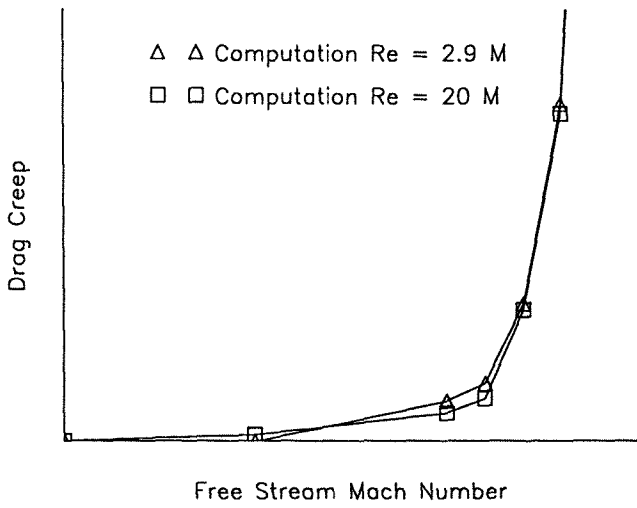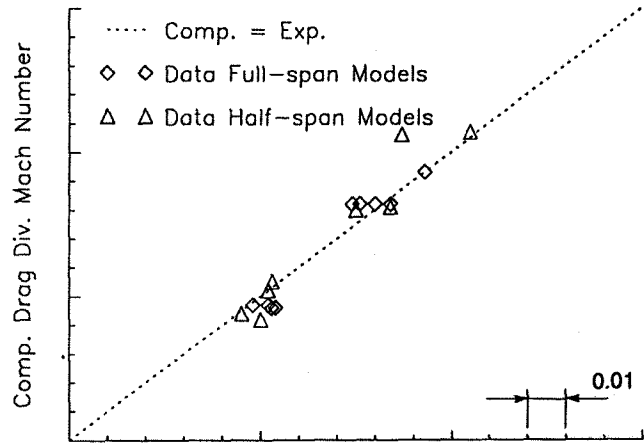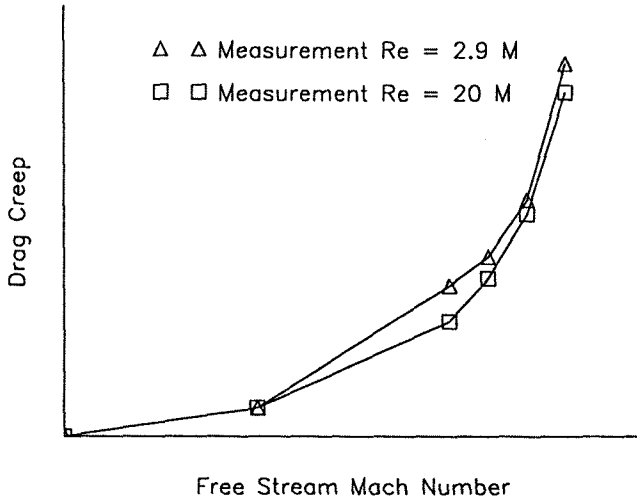Fig. 8c   Spatial distribution of wave drag at approx. 75% span for the DLR - F4 wing/body at $M_\infty = 0.75$, $C_L = 0.5$, $Re = 3*10^6$

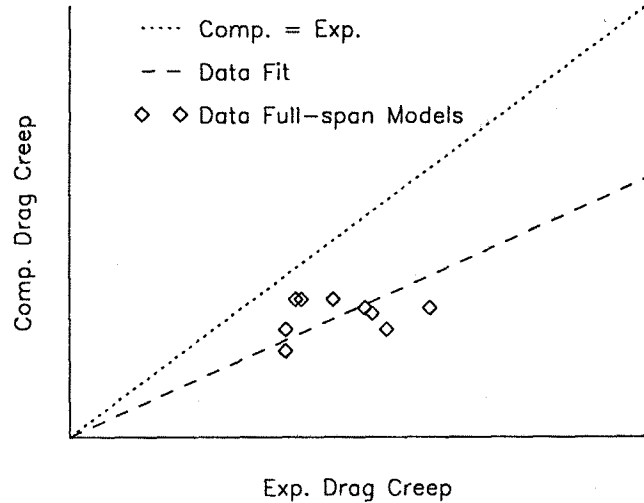**Fig. 9a** *Computed drag-creep for the Fokker 100 wing/body at $C_L = 0.5$*

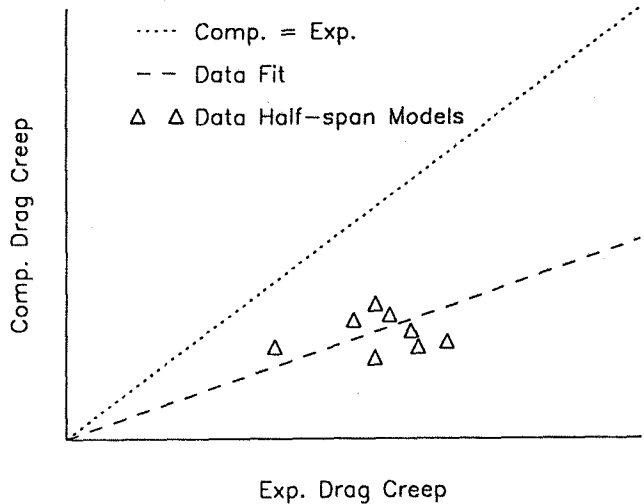**Fig. 9b** *Measured drag-creep for the Fokker 100 wing/body at $C_L = 0.5$*

Fig. 10a *Statistical correlation of experimental and computed drag-divergence Mach numbers for various wing/body configurations*

Fig. 10b *Statistical correlation of experimental and computed drag-creep at the drag-divergence Mach number for full-span wind tunnel models*

Fig. 10c *Statistical correlation of experimental and computed drag-creep at the drag-divergence Mach number for half-span wind tunnel models*

5 References

1). Steinle, F., Stanewsky, E., Wind Tunnel Flow Quality and Data Accuracy Requirements, AGARD-AR-184, November 1982.

2). McCroskey, W.J., A Critical Assessment of Wind Tunnel Results for the NACA 0012 airfoil, AGARD-CP-429, July 1988.

3). Boersen, S.J., Elsenaar, A., Half-Model Testing in the NLR High Speed Tunnel HST: its Technique and Application, NLR-MP-83036 U, 1983.

4). Henne, P.A., Gregg, R.D, New Airfoil Design Concept, J. Aircraft, Vol.28, No.5, May 1991.

5). Vooren, J. van der, Slooff, J.W., CFD-Based Drag Prediction; State-of- the-Art, Theory, Prospects. In: Drag-Prediction and Measurement; Lecture notes of AIAA Professional Studies Series, August 23-24, 1990, Portland, Oregon, USA; also NLR TP 90247, 1990.

6). Vooren, J. van der, Wees, A.J. van der, Inviscid Drag Prediction for Transonic Transport Wings Using a Full-Potential Method, J. Aircraft, Vol.28, Nr.12, December 1991.

7). Garabedian, P.R., Computation of Wave Drag for Transonic Flow, Journal d'Analyse Mathematique, Vol.30, pp. 164-171, 1976.

8). Destarac, D., Far-Field Drag in Transonic Potential Flow: Analysis and Optimization, ONERA-TP-1993-135, 1993.

9). Nikfetrat, K, Dam, C.P. van, Vijgen, P.M.H.W., Chang, I.C., Prediction of Drag at Subsonic and Transonic Speeds Using Euler Methods, AIAA-92-0169, January 1992.

10). Wees, A.J. van der, Muijden, J. van, A Robust Quasi-Simultaneous Interaction Method for a Full Potential Flow with a Boundary Layer with Application to Wing/Body Configurations. In: Proceedings 5th Symp. on Num. and Phys. Aspects of Aerodynamic Flows, Long Beach, California, January 13-15, 1992.

11). Tysell, L.G., Hedman, S.G., Towards a General Three-Dimensional Grid Generation System, ICAS-88-4.7.4, 1988.

12). Wees, A.J. van der, Muijden, J. van, Vooren, J. van der, A Fast and Robust Viscous-Inviscid Interaction Solver for Transonic Flow about Wing/Body Configurations on the Basis of Full-Potential theory, AIAA-93-3026, July 1993.

13). Cousteix, J., Three-Dimensional Boundary Layers, Introduction to Calculation Methods. In: Computation of Three-Dimensional Boundary Layers Including Separation, AGARD-R-741, 1987.

14). Houwink, R., Veldman, A.E.P., Steady and Unsteady Separated Flow Computations for Transonic Airfoils, AIAA-84-1618, 1984.

15). Green, J.E., Weeks, D.J., Brooman, J.W.F., Prediction of Turbulent Boundary Layers and Wakes in Compressible Flow by a Lag-Entrainment Method, ARC-R&M No. 3791, January 1973.

16). Hartwich, P.M., Split Coefficient Matrix (SCM) Method with Floating Shock Fitting for Transonic Airfoils, Proc. Int. Conf. on Num. Meth. in Fluid Dynamics, Oxford, July 1990.

17). Lock, R.C., Williams, B.R., Viscous-Inviscid Interactions in External Aerodynamics, Prog. Aerospace Sci., Vol. 24, 1987.

18). Kernkamp, G.J., Evaluation and Extension of the Mathematical Model Underlying the ISES-code, NLR Report to be published, 1994.

19). Drela, M., Giles, M.G., Viscous-Inviscid Analysis of Transonic and Low Reynolds Number Airfoils, AIAA Journal, Vol. 25, No.10, October 1987.

20). Redeker, G., Mueller, R., Ashill, P.R., Elsenaar, A., Schmitt, V., Experiments on the DFVLR-F4 Wing Body Configuration in Several European Wind Tunnels, AGARD-CP-429, July 1988.